Journal of Materials Chemistry A

Accepted Manuscript

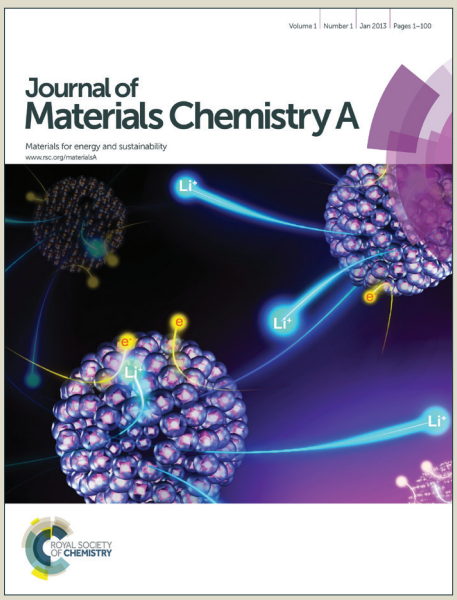

ROYAL SOCIETY OF CHEMISTRY

www.rsc.org/materialsA

Cite this: DOI: 10.1039/c0xx00000x

www.rsc.org/xxxxxx

ARTICLE TYPE

Template-directed synthesis of pyrite FeS_2 nanorod arrays with enhanced photoresponse

Mudan Wang[a], Chengcheng Xing[a], Ke Cao[a], Lei Zhang[b], Jiabin Liu*[a] and Liang Meng*[a]

Received (in XXX, XXX) Xth XXXXXXXXX 20XX, Accepted Xth XXXXXXXXX 20XX
DOI: 10.1039/b000000x

High solar conversion efficiency is the key for any semiconductor material to be a candidate for photovoltaic application. Although pyrite iron sulfide has become a promising candidate because of its extremely high light absorption coefficient, its solar conversion efficiency still remains below 3%. Herein, a novel 1-D pyrite nanostructure is designed to enhance the photoresponse properties. Well aligned pyrite nanorod arrays are successfully grown on fluorine doped tin oxide transparent and conductive glass substrate with a template-directed method. ZnO nanorod arrays are used as initial template to produce $Fe(OH)_3$ nanotube arrays and then the $Fe(OH)_3$ nanotube arrays are used as template to produce pyrite nanorod arrays. The pyrite nanorods have an average diameter of 130 nm and length of 600 nm. The prepared pyrite nanorod films exhibit outstanding light absorption and enhanced photocurrent in comparison with nanoparticle FeS_2 films. The excellent optical and photoelectrical performance of FeS_2 nanorod films is attributed to the unique 1-D ordered architecture, which has large surface areas for light harvest and provides a direct and short pathway for charge transport and reduces combination loss of photoelectrons. The method offers a new strategy for designing nanostructured materials with 1-D ordered architecture for high-performance photovoltaic devices.

1 Introduction

Pyrite iron sulfide (FeS_2) has recently become a promising candidate in this field and has been receiving continuous attention due to its many excellent properties. Extremely high light absorption coefficient (> 10^5 cm^{-1} for hv > 1.3 eV) and an appropriate bandgap (Eg = 0.95 eV) and, most importantly, the advantages of earth abundance (iron is the fourth most abundant element in the earth's crust), non toxicity and low cost make pyrite the highest-availability photovoltaic candidate among 23 types of existing semiconducting photovoltaic systems [1] that could potentially lead to lower cost compared to conventional silicon solar cells. Besides, pyrite has been an attractive thin-layer absorber material for photovoltaic [2, 3] and photoelectrochemical [4, 5] applications. To date, there have been series of researches on the preparation and photoelectronic properties of high-purity pyrite FeS_2 with different nanostructures, like nanocrystal ink, [6, 7]nanocube, [8, 9] nanowire/nanorod. [10-13] Moreover, some developed methods, such as control of sulfur chemical potential, [13] hot-injection route [14, 15] and introduction of metal oxide layers, [16] provide great probability for low-cost, large-area, solution-based processing of pyrite thin films for photovoltaic. Despite its attractive properties, the great limitation to pyrite's widespread application in photovoltaic devices is the low solar conversion efficiency, which has remained below 3% [17] for any pyrite-based solar devices. The main reason is attributed to the phase impurity or sulfur vacancies in the bulk and/or at the surface, which generates electronic states within the bandgap. [18] Many efforts based on the synthesis, [19-22] surface passivation, [23] and structural and photoelectronic characterization [24-26] of pyrite films have been devoted to enhancing photovoltaic performance and efficiency of pyrite cells. However, the results show little help to conversion efficiency. The preparation of phase-pure and high-efficiency FeS_2 film is still a huge challenge at present. Since the problem of low efficiency cannot be overcome easily with present technologies, conquering it from another different way, namely, by designing of material morphology to enhance photoelectric conversion, may be a nice consideration. Furthermore, successful studies of nanostructures from some other semiconductors such as Si, [27-34] CdTe, [35] and CdS/Cu_2S [36] suggest that 1-D nanostructures have various unique properties over planar geometries for solar applications. [33, 37]

Sufficient light absorption is a prerequisite for any semiconductor material to be a candidate for PV applications. Though it is mainly determined by the band gap of semiconductor, yet it can be significantly enhanced through other approaches. The most efficient way is to enlarge the surface areas

for light harvest by structure design. Aligned 1-D nanostructure arrays would be the preferred choice due to its unique structure features, such as extremely large surface areas as well as high junction areas and direct pathway for charge transport, endowing them with superior optical absorption properties compared with nanoparticle thin films. For example, the photocurrent in ZnO nanowire array films showed 50%-75% higher than that in ZnO nanoparticle films. [38] The mobility of electrons in 1-D nanostructures, such as carbon nanotube [39] and Ge, [40] Si [41] nanowires, is typically several orders of magnitude higher than that in their respective nanoparticle films. If pyrite FeS_2 can be prepared into forest-like aligned arrays, it will remarkably increase the surface areas for receiving sunlight illumination and, hence, obtain sufficient absorption of photons and enhanced photoelectric properties.

Up to now, preparation of well-aligned 1-D FeS_2 arrays is still an idea in mind, specifically on fluorine doped tin oxide (FTO) transparent and conductive glass substrate. Such configuration with arrays grown on FTO substrate can be directly used as photoanodes for solar cells and allows the complete transmission of sunlight. In this paper, a new strategy is developed to design nanostructure architecture of pyrite FeS_2. Vertically aligned FeS_2 nanorods are successfully grown on FTO substrate for the first time based on a template-directed synthesis using ZnO nanorod arrays (ZNAs) as the template and subsequent low-temperature sulfidation. The aligned FeS_2 nanorods exhibit much better photoelectric properties than the FeS_2 nanoparticles.

2 Results

The phase evolution during synthesis process was determined by X-ray diffraction (XRD). ZnO nanorod arrays with [1000] preferential direction is obtained and used as the initial template (Figure 1a). After ZnO template immersed in Fe^{3+} solution for 30 min, the crystallinity of ZnO nanorods is lowered (Figure 1b). The crystallinity of ZnO nanorods is continuously lowered with the prolongation of immersion time and ZnO diffractions peaks nearly disappear completely at the immersion time of 1 h (Figure 1c and 1d). No peak related to $Fe(OH)_3$ appears in the XRD pattern, indicating the $Fe(OH)_3$ should be amorphous which is commonly observed in wet-chemical reactions. [42, 43] After the immersion stage, the resulting $Fe(OH)_3$ film was annealed with sublimed sulfur powder at 350 °C for 3 h. The XRD results fully confirm that the final product FeS_2 has been successfully obtained (Figure 1e).

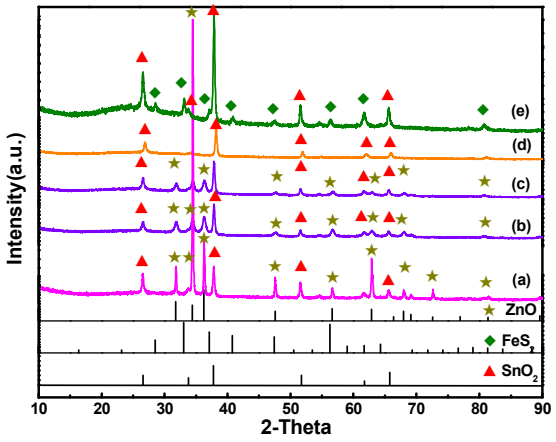

Fig.1 XRD patterns of (a) as-prepared ZnO template, and ZnO template immersed in Fe3+ solution for (b) 30 min, (c) 45 min and (d) 1 h, and (e) the final product after sulfurization.

The final FeS_2 films were obtained *via* three main processes including hydrothermal growth of ZnO template, immersion of the template in Fe^{3+} solution and sulfurization of solution-immersed films. The morphologies of products obtained after each process were investigated by SEM. Uniform, dense and well-oriented ZnO nanorod arrays were successfully grown on FTO substrate (Figure 2). The ordered ZnO nanorods are uniform with diameters ranging from 50 nm to 80 nm and length up to 3 μm. According to the former XRD result (Figure 1) and previous works, [44, 45] those ZnO nanorods grow with *c*-axis perpendicular to the substrate.

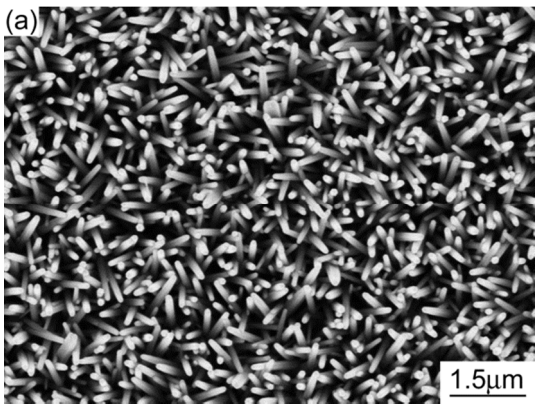

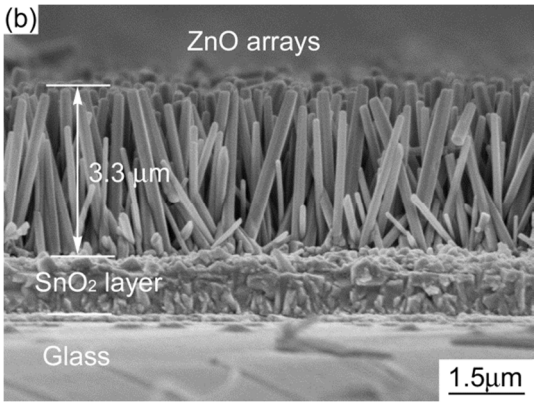

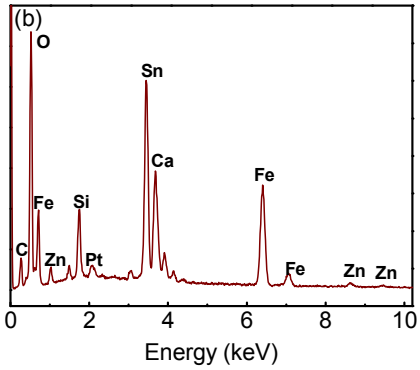

Fig.2 SEM images of the as-prepared ZNAs (a) top view and (b) cross-section view.

The morphology of the product immersed in Fe^{3+} solution for 1 h was given in Figure 3. The original ordered array structure is well preserved. The single-crystalline ZnO nanorods are transformed into $Fe(OH)_3$ nanorods made of multi-particles. Some $Fe(OH)_3$ nanorods have a hollow structure, which indicates that the nanorods should be nanotubes with tips closed. The outer diameters of nanotubes range from 80 to 120 nm and the inner diameters range from 30 to 50 nm. The chemical composition of $Fe(OH)_3$ nanotube film was characterized by EDS. The EDS spectrum shows the presence of Fe, O and trace amount of Zn element, which means that ZnO template is basically acid etched entirely and almost completely replaced by $Fe(OH)_3$. The signal of C element mainly comes from surface adsorption and contamination. The signal of Pt element comes from the sputter coating of Pt during SEM sample preparation. The coating treatment aims to gain better conductivity and clear SEM observation. The rest elements, Si, Sn and Ca, are from the FTO glass substrate. The relative contents of Zn, Fe and O elements of the samples immersed in Fe^{3+} solution for different time were calculated and shown in Figure 3c. The relative content of Zn decreases quickly at initial and then slowly, while the relative content of Fe increases quickly at initial and then also slowly. The increase of the relative content of O at initial period is due to the fact that three oxygen atoms combine with an iron atom in $Fe(OH)_3$. It should be pointed out that some signal of O element may come from the FTO substrate.

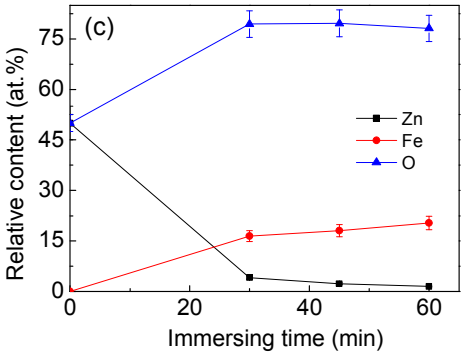

Fig.3 (a) Top-view SEM image and (b) EDS result of $Fe(OH)_3$ nanotube arrays obtained by immersed in Fe^{3+} solution for 1 h, (c) the change of the relative contents of Zn, Fe and O elements with different immersing time.

The morphology of the FeS_2 arrays obtained by sulfurizing the $Fe(OH)_3$ nanotube arrays is shown in Figure 4. The FeS_2 nanorods orient normal to the FTO substrate and the original 1-D ordered arrays are still preserved. The diameter of FeS_2 nanorods ranges from 120 to 140 nm with a length from 500 to 800 nm. The aspect ratio of FeS_2 nanorods is reduced when compared to that of ZnO nanorods.

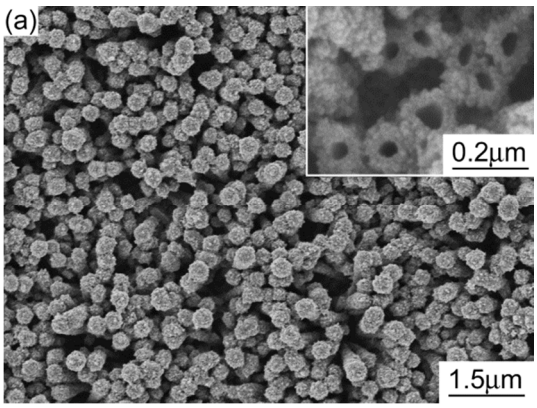

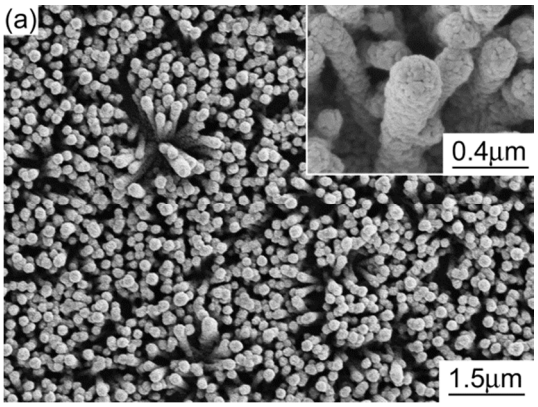

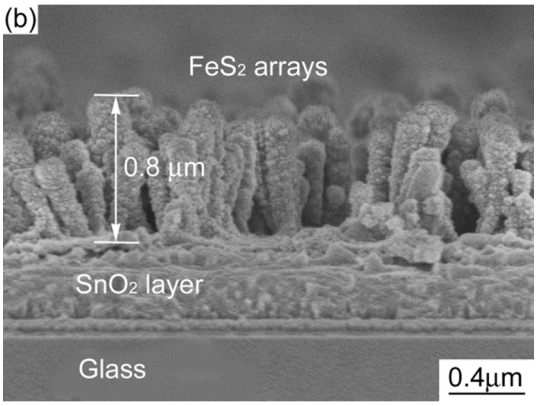

Fig.4 SEM images of the FeS_2 nanorod arrays (a) top view and (b) cross-section view.

The microstructure of the FeS_2 nanorod arrays was further investigated in transmission electron microscope (TEM) and shown in Figure 5. The rod morphology is still visible although the sample was ultrasonic dispersed for 15 min (Figure 5a). However, the rods seem loose in some content compared with those in SEM images (Figure 4). The select area electron diffraction (SAED) patterns show several sharp rings, which are well identified to (200), (211), (220), (221) and (311) of pyrite FeS_2 (Figure 5b). The corresponding dark-field image clearly shows that the rods consist of FeS_2 crystals (Figure 5c). The high crystallinity of FeS_2 is further directly confirmed by the high-resolution TEM image (Figure 5d). Regular arrangement of atoms is clearly observed and little lattice defect is found in the grain.

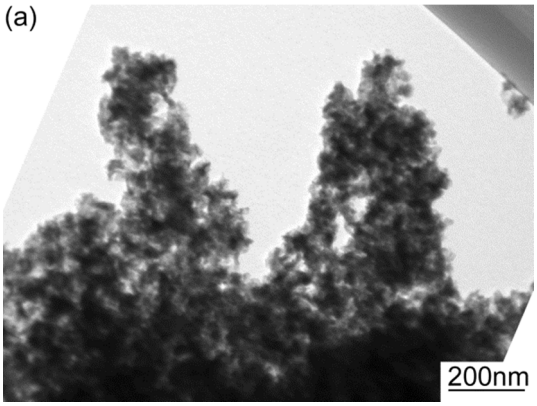

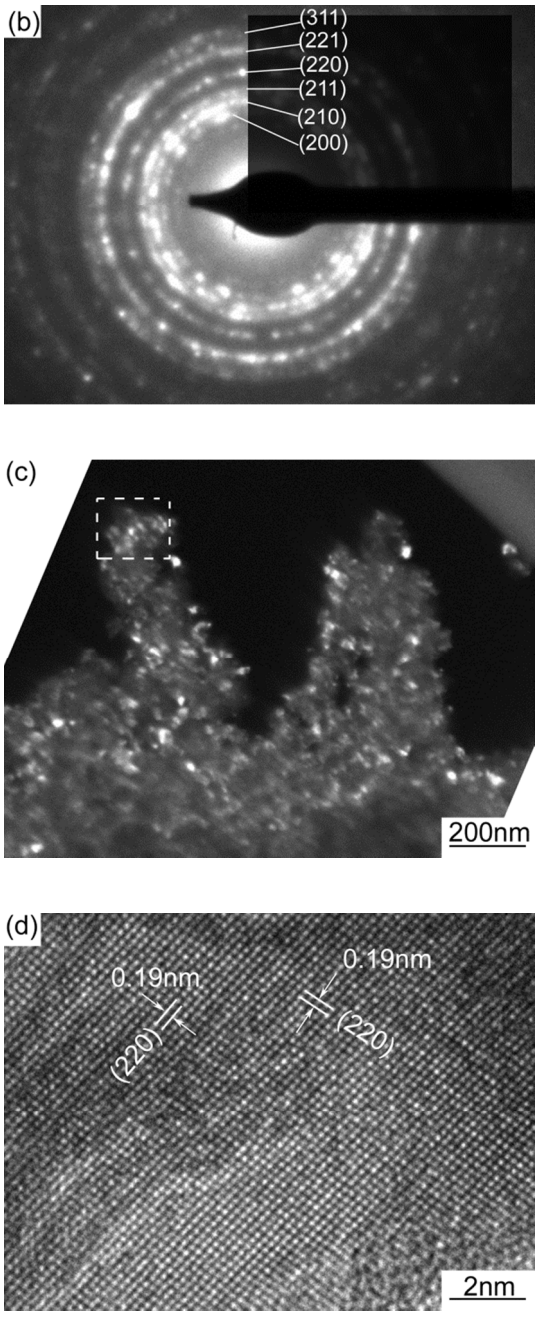

Fig.5 (a) Bright-field TEM image, (b) corresponding SAED patterns, (c) corresponding dark-field TEM image and (d) HRTEM image corresponding to the dash rectangle in (c) of the FeS_2 nanorods.

XPS tests were carried out to investigate the surface components of the FeS_2 nanorod films. From the survey scan (Figure 6a), it is clearly shown that the sample consists mainly of iron and sulfur. The signals corresponding to oxygen and carbon originate from surface adsorption and contamination. Figure 6b presents the Fe 2p spectrum of the FeS_2 nanorods. Two peaks located at 707.2 eV and 720.1 eV [46, 47] are attributed to the Fe $2p_{3/2}$ and Fe $2p_{1/2}$ binding energies in pyrite FeS_2, respectively. Figure 6c presents the S 2p spectrum of the FeS_2 nanorods. Two photoelectron signals observed at 162.6 eV and 163.7 eV, [13, 48]

corresponding to S $2p_{3/2}$ and S $2p_{1/2}$, are also consistent with the sulfur binding energy in pyrite FeS_2. It is suggested that there should be trace amount of FeS since an additional small S peak at 161.4 eV [49] is detected. The reason why FeS phase does not appear in the XRD pattern (Figure 1) is probably due to the low content of FeS which may be under the detection limit of XRD. According to the XPS analysis, the atomic ratio of Fe to S on the film surface is determined to be 1:1.7, which is deviated from the theoretical ratio (Fe:S=1:2). Preparation of pyrite FeS_2 with high purity, single phase and stoichiometric FeS_2 arrays is still a challenge at the present stage.

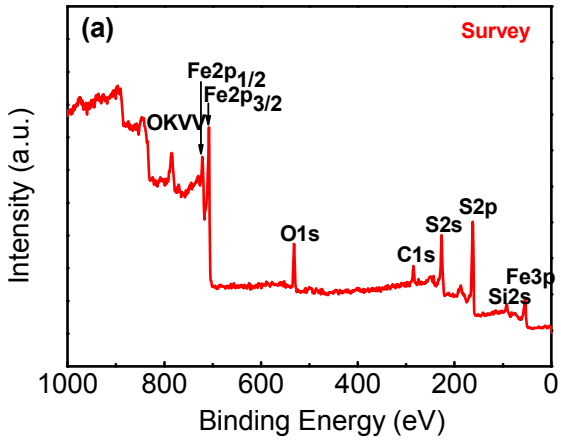

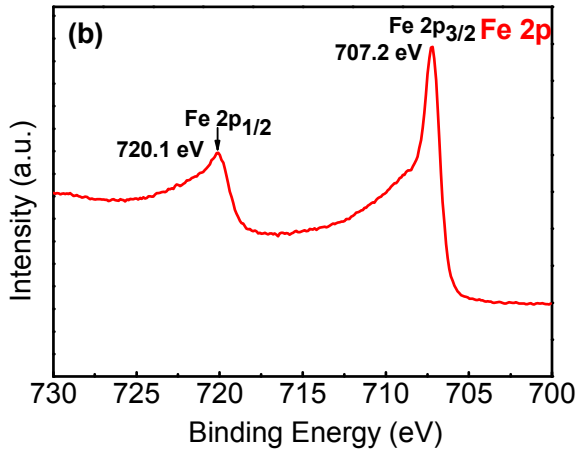

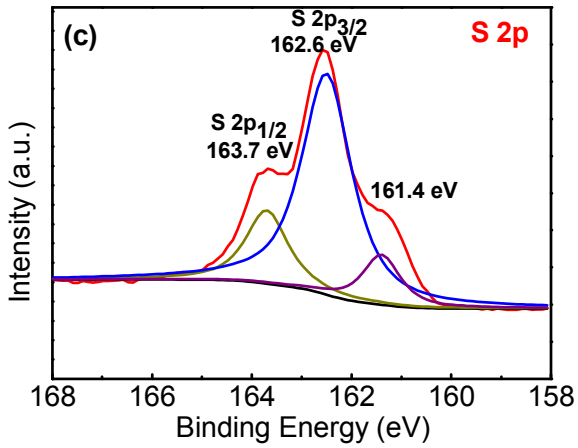

Fig.6 XPS analysis of the FeS_2 nanorods. (a) survey scan, and high resolution scans of (b) Fe region and (c) S region.

The Raman spectrum of the FeS_2 nanorods is shown in Figure 7. Two strong peaks located at 335 and 368 cm^{-1}, as well as a weak vibration band at 422 cm^{-1}, are clearly observed in Figure 7a. These peaks are the characteristic active modes for pyrite corresponding to the stretching of S_2 dumb-bells (A_g), the libration of S atom perpendicular to the dumb-bells axes (E_g), and coupled libration and stretch (triply degenerate, specifically $T_{g(3)}$) modes, [50] respectively. Actually, there are five Raman active modes ($A_g+E_g+3T_g$) in total for pyrite FeS_2 due to its symmetry structure of space group Pa3. [51] The frequency of T_g mode is very close to that of A_g mode. Here, only one T_g mode was observed at 422 cm^{-1} and the other two modes could be buried in the A_g mode at 368 cm^{-1}. Although FeS has been detected in former XPS characterization, it is not able to distinguish the FeS from FeS_2 by Raman due to their structural symmetry. [51]

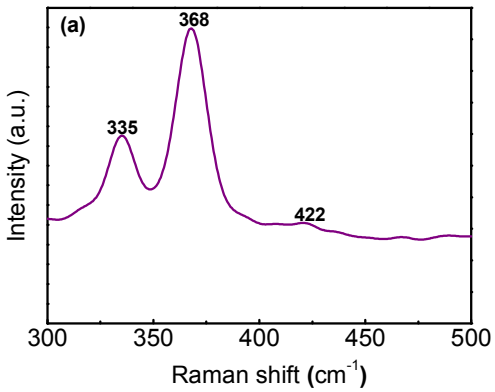

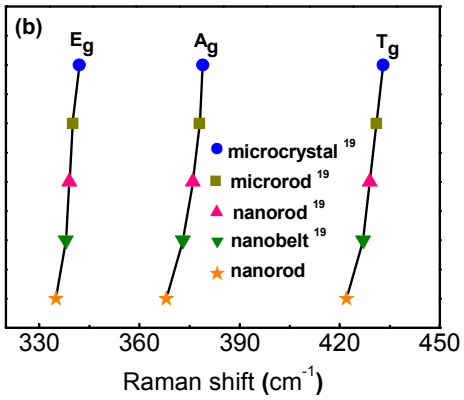

Fig.7 (a) Raman spectrum of FeS_2 films ($\lambda_{incident}$ = 532 nm) and (b) a red-shift for the Raman peaks of pyrite FeS_2 with different morphology.

Table 1 summarizes the specific Raman data of pyrite FeS_2 with different morphologies and characterization sizes. [17] An obvious red-shift of Raman peaks is found for pyrite FeS_2 as the crystal size reduces from micrometers to nanometers (Figure 7b). The reason for the observed red-shift may be related to the characterization dimension of the nanostructure. It is found that this red-shift becomes more obvious as the dimension of the nanostructure becomes smaller. Interestingly, a more evident peak shift for the A_g mode in comparison to the E_g mode is observed, which reflects the weaker bond strength for S-S in comparison to Fe-S.

Table 1. Raman shift for pyrite films with different morphologies and characterization dimensions.

Morphology	Characterization dimension (nm)	E_g	A_g	T_g	Reference
Microcrystal	2000	342	379	433	19
Microrod	1700	340	378	431	19
Nanorod	300	339	376	429	19
Nanobelt	300	338	373	427	19
Nanorod	140	335	368	422	This work

Pyrite regarded as a promising solar material is largely due to its favourable optical properties. Figure 8 shows the optical absorption spectrum of the FeS_2 nanorods. Both coefficient (α) and optical band gap (E_g) are determined from transmittance and reflectance measurements using an ultraviolet and visible spectrophotometer. The FeS_2 nanorods exhibit a high absorption coefficient with $\alpha > 10^5$ cm^{-1} in the visible range (Figure 8a). A wide absorption peak in the range of 500-800 nm is observed for FeS_2 nanorods, which makes them possible to be the candidate material in photovoltaic devices. Moreover, in the regions of high absorption energy the absorption coefficients approximately reach stable values. The dependence of the absorption coefficient on photon energy near the absorption edge suggests that the band gap is indirect, as is expected from theoretical calculations. [52] The optical band gap can be estimated by the conventional Tauc equation: [53]

$$\alpha h\nu = A(h\nu - E_g)^n \quad (1)$$

where $h\nu$ is the photon energy; A is the constant; n=2 for an indirectly allowed transition and n=1/2 for a directly allowed transition. By fitting the absorption coefficient to the general formula for indirect allowed transitions, the value of the band gap energy is obtained. Figure 8b shows the graph of $(\alpha h\nu)^{1/2}$ vs photon energy $h\nu$ for FeS_2 nanorods. When the linear dependence of $(\alpha h\nu)^{1/2}$ on $h\nu$ is extrapolated to zero, it gives the optical band gap that is found to be 0.89 eV for FeS_2 nanorods.

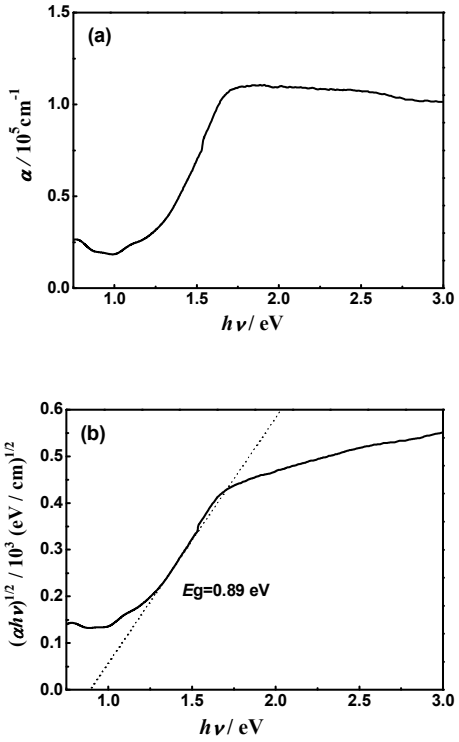

Fig.8 Optical absorption spectrum of the FeS_2 nanorods. (a) absorption coefficient and (b) Tauc plot of $(\alpha h\nu)^{1/2}$ vs $h\nu$ for the estimation of band gap.

The photocurrent-potential (I-V) behavior of the FeS_2 nanorod electrode was measured under irradiation with a Xenon lamp at an intensity of 500 mW cm^{-2} in a three-electrode photoelectrolysis cell with 0.5M Na_2SO_4 solution as electrolyte, FTO substrate with FeS_2 nanorod film as working electrode, a Pt foil as counter electrode, and a saturated calomel electrode (Hg/Hg_2Cl_2/sat. KCl) as reference electrode, separated by glass frits. Contact to the working electrode was made with a Cu clip wire above the electrolyte. During the whole experiment process, the three-electrode cell was kept still and the tests under light and dark were achieved by controlling the on/off state of Xenon lamp. Figure 9 displays the photocurrent against the potential for FTO

substrate, FeS_2 nanorods and FeS_2 nanoparticles as comparison under darkness and simulated sunlight, respectively. The current of FTO substrate isn't detected under both of darkness and sunlight from -1.0 V to 1.0 V. The I-V curve under darkness almost entirely overlaps with that of under illumination, which suggests that the bare FTO substrate have no photoelectric response. In the case of natural pyrite electrode, it is difficult to observe a photocurrent. [47] However, after growth of pyrite FeS_2 nanorods on the FTO substrate, a significant photocurrent is observed and the current steadily increases as the potential increases from 0.4 to 1.0 V for both the positive and negative side. It is reasonable that the anodic photocurrent generated increases with the increasing applied potential, as the FeS_2 is a typical *n*-type semiconductor. Compared with FeS_2 nanorods, much weaker photoresponse was observed for FeS_2 nanoparticles with the same potential under dark and illumination conditions. It is obvious that the FeS_2 nanorods have a prominent photocurrent, which is much higher than that of FeS_2 nanoparticles. Hence, it can be concluded that 1-D nanostructures perform excellent superiority and promising prospects in PV application. [54, 55]

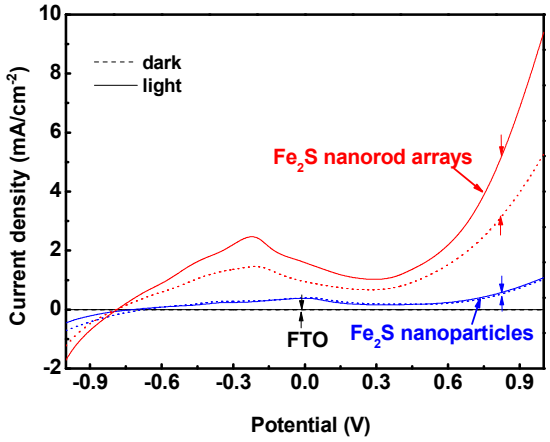

Fig.9 Photocurrent-potential behavior of FeS_2 films under the dark and illumination, respectively. The data were collected as a single sweep from negative to positive potentials ranging from -1.0 to 1.0 V. The anode was irradiated using a xenon lamp at an intensity of 500 mW cm^{-2} in a three-electrode system in 0.5M sodium sulfate solution.

The stability is also an important concern for pyrite FeS_2 nanomaterials due to its susceptibility to oxidation and decomposition. The stability of pyrite FeS_2 is determined to some extent by the preparation methods. For solution-processable pyrite FeS_2 nanocrystals (NCs), the NCs solution show complete decomposition within weeks for storage in air, [14] forming a yellow precipitate and clear supernatant. Surfactants, like TOPO, [56] P_3HT [57] and PCBM, [58] are regularly applied to capped with the NCs in solution preparation, inhibiting the rapid degradation of pyrite FeS_2 NCs accelerated by nano effect. Pyrite NC thin films without post-heat treatment are observed to change color within a few weeks in air and show impurity peaks in XRD pattern with exposure to air for 3 months.[15] While for pyrite FeS_2 films with sintering treatment, the polycrystalline pyrite films are stable for at least 1 month in air without discoloration or the appearance of new phases in XRD patterns. [14] The stability of the pyrite FeS_2 nanorod films prepared by our template-directed method combined with subsequent sulfidation are stable for at least 1 year in a vacuum drier with no discoloration and no apparent change in the XRD patterns (figure S3). Air stability and detailed analysis and mechanism of the decomposition still require further extensive researches.

3 Discussion

3.1 Growth of FeS_2 nanorod arrays

The growth of FeS_2 nanorod arrays is schematically illustrated in Scheme 1. Firstly, a well-aligned ZNAs template is grown on ZnO-coated FTO substrate *via* hydrothermal method (Figure 2). Secondly, the obtained ZNAs are used as the initial template and immersed in $Fe(NO_3)_3$ aqueous solution. Fe^{3+} begins to hydrolyze and produces $Fe(OH)_3$ colloid and H^+. The hydrolysis occurs preferentially around the ZnO nanorods which also serve as a "patterned" substrate to support the $Fe(OH)_3$ colloid. Simultaneously, the ZnO nanorods are etched by H^+. This consumption of H^+ accelerates the hydrolysis reaction of Fe^{3+}, leading to an enhanced hydrolysis in the vicinity of the ZnO nanorods. As a result, the precipitation of $Fe(OH)_3$ emerges on the scaffold of ZnO nanorods, forming the early rigid base of nanotubes. Progressive hydrolysis and template dissolution eventually result in well-oriented $Fe(OH)_3$ nanotubes (Figure 3). The two chemical reactions of the hydrolysis and acid etching occurred in the immersion process are formulated as follows: [42]

$$Fe^{3+}+3H_2O \rightarrow Fe(OH)_3+3H^+ \quad (2)$$

$$ZnO+2H^+ \rightarrow Zn^{2+}+H_2O \quad (3)$$

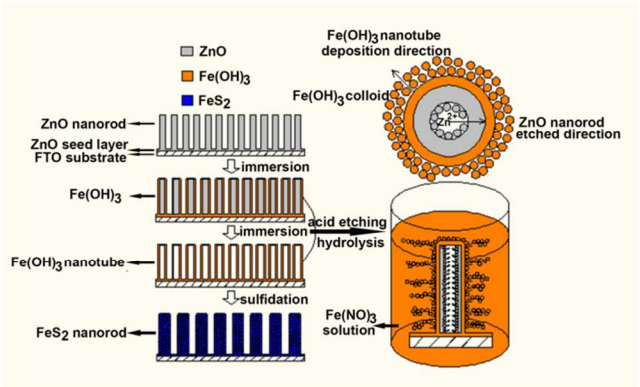

Scheme 1 Schematic diagram for the fabrication process of FeS_2 nanorod arrays.

The prepared $Fe(OH)_3$ nanotube arrays also serve as a template and react with sulfur powder in an sealed quartz ampoule. The sulfur atoms diffuse continuously into the $Fe(OH)_3$ nanotube and take reaction with $Fe(OH)_3$. The detailed reaction is described as follows:

$$4Fe(OH)_3+11S \rightarrow 4FeS_2+6H_2O+3SO_2 \quad (4)$$

In the template-directed synthesis, ZnO template has two functions: first, it is a removable/sacrificial template for the formation of $Fe(OH)_3$ nanotubes; second, the *in-situ* dissolution exerts an acceleration effect on the hydroxide precipitation. During the solution-immersion stage, the produced $Fe(OH)_3$ colloids prefer to deposit on the outer wall of ZnO nanorod and gradually form $Fe(OH)_3$ layer along the radial direction to outward. The final $Fe(OH)_3$ nanotube morphology can be obtained by removing the ZnO nanorod template, which is determined by the crystal structure of wurtzite ZnO. Compared with the nonpolar planes parallel to the *c* axis, two polar planes, *i.e.*, (0001) and $(000\bar{1})$ planes, have higher surface energy and are metastable. Additionally, it is proposed that more defects were formed in the inner part of ZnO nanorod. [59] Hence, the etching will preferentially occur in the (0001) planes along the *c* axis by H^+ derived from the hydrolysis of Fe^{3+}, and the etching rate is much faster than that of the nonpolar planes. As a result, the ZnO nanorods are completely removed out and $Fe(OH)_3$ nanotube arrays are obtained. In the aspect of designing hollow structures, Galvanic replacement, applied to the fabrication of metal [60] and metallic oxide [61] with hollow structure, has been regarded as a simple and versatile route with tunable morphologies and controllable compositions. By coupling our template-directed synthesis with the galvanic replacement, it is possible and promising to obtain more complex and innovative structures beyond expectation, which will provide unique properties and enhanced performances in certain fields.

3.2 Photoelectric properties of FeS_2 nanorod arrays

The major barrier to the structure and photoefficiency of nanoparticle films for application in solar cells is the convoluted internal interface and a high degree of structural disorder. The most efficient alternative strategy to solve the two problems is introducing well-aligned 1-D nanostructures. Hence, replacing the disordered nanoparticle architectures with ordered nanostructure arrays of optimal dimensions is a promising approach to boost the carrier collection yield and power conversion efficiency of nanostructured solar cells.

The photoelectric properties of FeS_2 films to a large extent are determined by the structure of films, which has a great influence on the surface area for light harvest and electron transport. Scheme 2 illustrates the difference in light harvest and electron transport for films with FeS_2 1-D nanostructures and nanoparticles, respectively. Compared with FeS_2 nanoparticle films, 1-D FeS_2 nanorod arrays possess a larger surface area for the absorption of sunlight and, therefore, the capture of enough incident photons. As to electron transport, a hopping mechanism, [62] which occurs between trap states on neighboring particles, has been proposed for the photoelectron transport in nanoparticle films. Besides, an electron is estimated to cross 10^3–10^6 particles when traveling in the photoelectrode film and usually trapped by isolated nanoparticles, surface states, or defect states. Although the FeS_2 nanorods prepared in this paper also compose of many nanoparticles (as can be seen from Figure 4 and Figure 5), the electron transport in the FeS_2 nanorods is different from that of FeS_2 nanoparticles. Due to its unique 1-D structure feature, the electrons are confined in the 1-D nanorod channel and transport along the axial direction from the point of electron injection to the substrate of the collection electrode, which largely reduce the scattering and combination loss of electrons. This differs from the case of nanoparticle films in a solar cell configuration, where electrons, during their traversal, take a random walk among the nanoparticles and undergo numerous collisions at the grain boundary. Hence, 1-D nanorod arrays structure, as well as nanotube, nanowire and nanobelt offer significant opportunities to improve efficiencies of solar cells by facilitating photo absorption, electron transport, and electron collection.

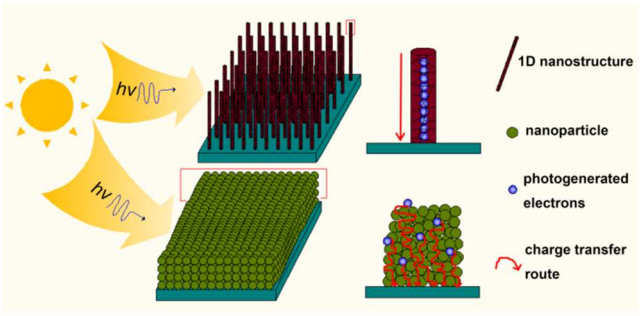

Scheme 2 A schematic illustration to indicate the difference in light harvest and electron transport for films with 1-D nanostructures and nanoparticles, respectively.

4 Conclusions

In summary, a novel facile strategy has been put forward for the fabrication of 1-D pyrite FeS_2 nanorod arrays. Large-area FeS_2 nanorods with well-oriented alignment were achieved on FTO substrate by using ZNAs as template. The prepared FeS_2 nanorod films exhibited outstanding light absorption and enhanced photocurrent in comparison with nanoparticle FeS_2 films. The excellent optical and photoelectrical performance of FeS_2 nanorod films is attributed to the unique 1-D ordered architecture, which has large surface areas for light harvest and provides a direct and short pathway for charge transport and reduces combination loss of photoelectrons. The method offers a new strategy for designing nanostructured materials with 1-D ordered architecture for high-performance photovoltaic devices.

5 Experimental Section

Chemicals: Zinc nitrate hexahydrate ($Zn(NO_3)_2{\cdot}6H_2O$, AR), hexamethylenetetramine (HMTA) ($C_6H_{12}N_4$, AR), zinc acetate dehydrate ($Zn(CHCOO)_2{\cdot}2H_2O$, AR), ethanolamine (MEA) ($NH_2CH_2CH_2OH$, AR), 2-methoxyethanol ($CH_3OCH_2CH_2OH$, AR), acetyl acetone ($C_5H_8O_2$, AR), iron nitrate nonahydrate

($Fe(NO_3)_3{\cdot}9H_2O$) and sulfur were used as received without any treatment. FTO glass with the dimension of 50 mm×15 mm×2 mm was used as substrate and was ultrasonically cleaned in acetone, ethanol and de-ionized water for 15 minutes each, respectively.

Synthesis of ZNAs: A seed solution with concentration of 1M was prepared by sol-gel method. Zinc acetate dehydrate and MEA of equivalent molar were dissolved in 2-methoxyethanol at ambient temperature. The mixture was magnetically stirred at 60 °C for 30 min to obtain a transparent and homogeneous solution. The substrates were dipped into the seed solution and pulled up at a rate of 200 mm min^{-1}, and then the coated substrates were dried at 80 °C in an oven. The procedure above was repeated three times. Finally, the substrates were heat-treated at 300 °C for 10 min and then heated to 550 °C at a rate of 2 °C min^{-1} for 1 h to obtain uniform and dense ZnO seed layers on the substrates.

A precursor solution for the growth of ZNAs was prepared by dissolving zinc nitrate hydrate ($Zn(NO_3)_2{\cdot}6H_2O$) with concentration of 0.025 M and HMTA ($C_6H_{12}N_4$) in de-ionized water. The molar ratio of Zn^{2+} to HMTA was 1:1. Then the precursor solution was put into a Teflon-lined autoclave of 25 ml capacity and the seed-coated substrates were put face down in the solution, and the autoclave was sealed and heated at 90 °C for 6 h. After the heating treatment, the autoclave was cooled to room temperature, and the substrates were removed from solution, rinsed with de-ionized water 2-3 times, and then dried in air.

Synthesis of FeS_2 nanorod films: The as-synthesized ZNAs used as template were first placed into an aqueous solution with $Fe(NO_3)_3{\cdot}9H_2O$ 0.27 g per 50 mL and kept still at room temperature for certain time. After immersion, it was taken out and dried in air. The solution-immersed films and sublimed sulfur powder with the amount calculated to produce 80 kPa sulfur pressure at annealing temperature were sealed in quartz ampoules. The ampoules were filled with pure argon and evacuated repeatedly five times before being sealed. To produce FeS_2 nanorods films, the sealed samples were finally isothermally annealed at 350 ^oC for 3 h.

Characterization: The film structural characterization was determined by X-ray diffraction diffractometer (XRD, X'Pert PRO) using Cu Kα radiation. The morphologies of the samples were investigated by a field-emission scanning electron microscopy (FESEM, Hitachi SU-70). TEM test was carried out in a Philips CM200 operated at 200 kV. The FeS_2 nanorod thin film was scraped from the FTO and dispersed in ethanol with ultrasonic dispersion for 15 min. Then several drops of the turbid liquid were transferred onto the Cu grid for TEM test. The Ultraviolet-visible (UV-vis) optical absorption measurements were performed on Hitachi U-4100 spectrophotometer. The ionic characteristics and surface composition were studied by X-ray photoelectron spectroscopy (XPS, Escalab 250Xi). A Renishaw inVia confocal Raman microscope with 532 nm laser excitation was used for Raman experiments. The photoelectro-chemical measurement was conducted in an electrochemical working station (CHI-660D) with a Xenon lamp at an intensity of 500 mW cm^{-2} in a three-electrode configuration photoelectrolysis cell. A 0.5M Na_2SO_4 solution was used as supporting electrolyte and the active area of the sample was 1.0 cm×1.0 cm.

Acknowledgements

This work has been supported by the National Science Foundation of China (Grant Nos. 51171022 and 21301155).

Notes and references

[a] *Department of Materials Science and Engineering, Zhejiang University, Hangzhou 310027, China. Fax: +86 57187953134; Tel: +86 57187953134; E-mail: liujiabin@zju.edu.cn; mengliang@zju.edu.cn.*
[b] *School of Materials Science and Engineering, University of Science and Technology Beijing, Beijing 100083, China.*
†Electronic Supplementary Information (ESI) available: [details of any supplementary information available should be included here]. See DOI: 10.1039/b000000x/

References

1 C. Wadia, A. P. Alivisatos and D. M. Kammen, *Environ. Sci. Technol.*, 2009, **43**, 2072-2077.
2 J. Hu, Y. Zhang, M. Law and R. Wu, *J. Am. Chem. Soc.*, 2012, **134**, 13216-13219.
3 L. Yu, S. Lany, R. Kykyneshi, V. Jieratum, R. Ravichandran, B. Pelatt, E. Altschul, H. A. S. Platt, J. F. Wager, D. A. Keszler and A. Zunger, *Adv. Energy Mater.*, 2011, **1**, 748-753.
4 J. Jiao, L. Chen, D. Kuang, W. Gao, H. Feng and J. Xia, *RSC Adv.*, 2011, **1**, 255-261.
5 X. Zhang, M. Manno, A. Baruth, M. Johnson, E. S. Aydil and C. Leighton, *ACS Nano*, 2013, **7**, 2781-2789.
6 Y. C. Wang, D. Y. Wang, Y. T. Jiang, H. A. Chen, C. C. Chen, K. C. Ho, H. L. Chou and C. W. Chen, *Angew. Chem. Int. Ed.*, 2013, **52**, 6694-6698.
7 K. Ramasamy, M. A. Malik, N. Revaprasadu and P. O'Brien, *Chem. Mater.*, 2013, **25**, 3551-3569.
8 W. Li, M. Döblinger, A. Vaneski, A. L. Rogach, F. Jäckel, J. Feldmann, *J. Mater. Chem.* 2011, **21**, 17946.
9 D. Wang, Q. Wang and T. Wang, *CrystEngComm*, 2010, **12**, 3797.
10 Q.-H. Huang, T. Ling, S.-Z. Qiao and X.-W. Du, *J. Mater. Chem. A*, 2013, **1**, 11828.
11 M. Caban-Acevedo, M. S. Faber, Y. Tan, R. J. Hamers and S. Jin, *Nano Lett.*, 2012, **12**, 1977-1982.
12 G. H. Yue, P. X. Yan, X. Y. Fan, M. X. Wang, D. M. Qu, D. Yan and J. Z. Liu, *J. Appl. Phys.*, 2006, **100**, 124313.
13 Y. Bai, J. Yeom, M. Yang, S.-H. Cha, K. Sun and N. A. Kotov, *J. Phys. Chem. C*, 2013, **117**, 2567-2573.
14 J. Puthussery, S. Seefeld, N. Berry, M. Gibbs and M. Law, *J. Am. Chem. Soc.*, 2010, **133**, 716-719.
15 Y. Bi, Y. Yuan, C.L. Exstrom, S.A. Darveau and J. Huang, *Nano Lett.*, 2011, **11**, 4953-4957.
16 D. Y. Wang, Y. T. Jiang, C. C. Lin, S. S. Li, Y. T. Wang, C. C. Chen and C. W. Chen, *Adv. Mater.*, 2012, **24**, 3415-3420.
17 C. Wadia, Y. Wu, S. Gul, S. K. Volkman, J. Guo and A. P. Alivisatos, *Chem. Mater.*, 2009, **21**, 2568-2570.
18 C. Steinhagen, T. B. Harvey, C. J. Stolle, J. Harris and B. A. Korgel, *J. Phys. Chem. Lett.*, 2012, **3**, 2352-2356.
19 M. Cab´an-Acevedo, D. Liang, K. S. Chew, J. P. DeGrave, N. S. Kaiser and S. Jin, *ACS Nano*, 2013, **7**, 1731-1739.
20 J. R. Ares, A. Pascual, I. J. Ferrer and C. Sánchez, *Thin Solid Films*, 2005, **480-48**, 477-481.
21 M.-L. Li, Q.-Z. Yao, G.-T. Zhou, X.-F. Qu, C.-F. Mu and S.-Q. Fu, *CrystEngComm*, 2011, **13**, 5936.
22 M. Akhtar, J. Akhter, M. A. Malik, P. O'Brien, F. Tuna, J. Raftery and M. Helliwell, *J. Mater. Chem.*, 2011, **21**, 9737.
23 M. Gong, A. Kirkeminde, N. Kumar, H. Zhao and S. Ren, *Chem. Commun.*, 2013, **49**, 9260-9262.
24 J. M. Lucas, C.-C. Tuan, S. D. Lounis, D. K. Britt, R. Qiao, W. Yang, A. Lanzara and A. P. Alivisatos, *Chem. Mater.*, 2013, **25**, 1615-1620.
25 M. Gong, A. Kirkeminde, Y. Xie, R. Lu, J. Liu, J. Z. Wu and S. Ren, *Adv. Opt. Mater.*, 2013, **1**, 78-83.

26 S. Shen, Y. Zhang, L. Peng, B. Xu, Y. Du, M. Deng, H. Xu and Q. Wang, *CrystEngComm*, 2011, **13**, 4572.

27 S. W. Boettcher, E. L. Warren, M. C. Putnam, E. A. Santori, D. Turner-Evans, M. D. Kelzenberg, M. G. Walter, J. R. McKone, B. S. Brunschwig, H. A. Atwater and N. S. Lewis, *J. Am. Chem. Soc.*, 2011, **133**, 1216-1219.

28 B. Tian, T. J. Kempa and C. M. Lieber, *Chem. Soc. Rev.*, 2009, **38**, 16-24.

29 S. K. Kim, R. W. Day, J. F. Cahoon, T. J. Kempa, K. D. Song, H. G. Park and C. M. Lieber, *Nano Lett.*, 2012, **12**, 4971-4976.

30 S. B. Michael, D. Kelzenberg, J. A. Petykiewicz, D. B. Turner-Evans, E. L. W. Morgan, C. Putnam, J. M. Spurgeon, R. M. Briggs, N. S. Lewis and H. A. Atwater, *Nat. Mater.*, 2010, **9**, 239-244.

31 M. D. Kelzenberg, D. B. Turner-Evans, M. C. Putnam, S. W. Boettcher, R. M. Briggs, J. Y. Baek, N. S. Lewis, H. A. Atwater, *Energ. Environ. Sci.*, 2011, **4**, 866.

32 G. Yuan, K. Aruda, S. Zhou, A. Levine, J. Xie and D. Wang, *Angew. Chem. Int. Ed.*, 2011, **50**, 2334-2338.

33 J. M. Foley, M. J. Price, J. I. Feldblyum and S. Maldonado, E *Energ. Environ. Sci.*, 2012, **5**, 5203.

34 Y. Dan, K. Seo, K. Takei, J.H. Meza, A. Javey, K.B. Crozier, *Nano Lett.*, 2011, **11**, 2527-2532.

35 R. Kapadia, Z. Fan and A. Javey, *Appl. Phys. Lett.*, 2010, **96**, 103116.

36 Z. Huo, J. Y. Tang, S. Brittman, H. W. Gao and P. D. Yang, *Nat. Nanotechnol.*, 2011, **6**, 568.

37 M. J. Bierman and S. Jin, *Energ. Environ. Sci.*, 2009, **2**, 1050.

38 M. Law, L. E. Greene, J. C. Johnson, R. Saykally and P. Yang, *Nat. Mater.*, 2005, **4**, 455-572.

39 S. A. G. T. Durkop, E. Cobas and M. S. Fuhrer, *Nano Lett.*, **2004**, **4**, 35-39.

40 D. Wang and H. Dai, *Appl. Phys. A*, 2006, **85**, 217-225.

41 D. V. Edwin, B. Ramayya, S. M. Goodnick and I. Knezevic, *IEEE T. Nanotechnol.*, **2007**, 6, 113-117.

42 J. Liu, Y. Li, H. Fan, Z. Zhu, J. Jiang, R. Ding, Y. Hu and X. Huang, *Chem. Mater.*, 2010, **22**, 212-217.

43 L. Qin, Q. Zhu, G. Li, F. Liu and Q. Pan, *J. Mater. Chem.*, 2012, **22**, 7544.

44 T. Ma, M. Guo, M. Zhang, Y. Zhang and X. Wang, *Nanotechnology*, **2007**, **18**, 035605.

45 J. Qiu, X. Li, W. He, S. J. Park, H. K. Kim, Y. H. Hwang, J. H. Lee and Y. D. Kim, *Nanotechnology*, 2009, **20**, 155603.

46 S. Seefeld, M. Limpinsel, Y. Liu, N. Farhi, A. Weber, Y. Zhang, N. Berry, Y. J. Kwon, C. L. Perkins, J. C. Hemminger and R. Wu, M. Law, *J. Am. Chem. Soc.*, 2013, **135**, 4412-4424.

47 X. Qiu, M. Liu, T. Hayashi, M. Miyauchi and K. Hashimoto, *Chem. Commun.*, 2013, **49**, 1232-1234.

48 J. Xia, J. Jiao, B. Dai, W. Qiu, S. He, W. Qiu, P. Shen and L. Chen, *RSC Adv.*, 2013, **3**, 6132.

49 R. Morrish, R. Silverstein and C. A. Wolden, *J. Am. Chem. Soc.*, 2012, **134**, 17854-17857.

50 L. Li, M. Cab´an-Acevedo, S. N. Girard and S. Jin, *Nanoscale*, 2014, **6**, 2112-2118.

51 L. Zhu, B. Richardson, J. Tanumihardja and Q. Yu, *CrystEngComm*, 2012, **14**, 4188.

52 T. K. Pietro, P. Altermatt, K. Ellmer and H. Tributsch, *Sol. Energ. Mat. Sol. C.*, 2002, **71**, 181-195.

53 J. Xia, X. Lu, W. Gao, J. Jiao, H. Feng and L. Chen, *Electrochim. Acta*, 2011, **56**, 6932-6939.

54 A. S. Aricò, P. Bruce, B. Scrosati, J. M. Tarascon and W. Van Schalkwijk, *Nat. Mater.*, 2005, **4**, 366-377.

55 Y. N. Xia, Y. G. Sun, Y. Y. Wu, B. Mayers, B. Gates, Y. D. Yin, F. Kim and H. Q. Yan, *Adv. Mater.*, 2003, **15**, 353-389.

56 S. C. Mangham, M. Alam Khan, M. Benamara and M. O. Manasreh, *Mater. Lett.*, 2013, **97**, 144-147.

57 C.W. Lin, D. Y. Wang, Y. T. Wang, C. C. Chen, Y. J. Yang and Y. F. Chen, *Sol. Energ. Mat. Sol. C.*, 2011, **95**, 1107-1110.

58 L. Zhu, B. J. Richardson and Q. Yu, *Nanoscale*, 2014, **6**, 1029-1037.

59 G.-W. She, X.-H. Zhang, W.-S. Shi, X. Fan, J. C. Chang, C.-S. Lee, S.-T. Lee and C.-H. Liu, *Appl. Phys. Lett.*, 2008, **92**, 053111.

60 X. Xia, Y. Wang, A. Ruditskiy and Y. Xia, *Adv. Mater.*, 2013, **25**, 6313-6333.

61 M. H. Oh, T. Yu, S. H. Yu, B. Lim, K. T. Ko, M. G. Willinger, D. H. Seo, B. H. Kim, M. G. Cho, J. H. Park, K. Kang, Y. E. Sung, N. Pinna and T. Hyeon, *Science*, 2013, **340**, 964-968.

62 N. K. K. D. Benkstein, J. van de Lagemaat and A. J. Frank, *J. Phys. Chem. B*, 2003, **107**, 7759-7767.

Graphical abstract

Well-aligned ZnO nanorod array was used as template to produce $Fe(OH)_3$ nanotube array. Then the as-grown $Fe(OH)_3$ nanotube array was used as template to obtain the FeS_2 nanorod array. The FeS_2 nanorod array exhibited much better photovoltaic properties than the FeS_2 nanoparticles due to the high specific area, direct transport pathways and enhanced light harvesting of nanorod array structure.